Elongational behaviour of electrostatically stabilised and concentrated CNF and CNC hydrogels: Experiments and modelling

Pierre J.J. Dumont, Shubham Gupta, Florian Martoïa, Laurent Orgéas

Elongational behaviour of electrostatically stabilised and concentrated CNF and CNC hydrogels: experimental aspects and modelling

P.J.J. Dumont[1]*, S. Gupta[1,2], F. Martoïa[1], L. Orgéas[2]
[1]*Univ. Lyon, INSA-Lyon, CNRS, LaMCoS, UMR5259, 69621 Villeurbanne, France*
[2]*Univ. Grenoble Alpes, CNRS, Grenoble INP, 3SR Lab, F-38000 Grenoble, France*

*Corresponding author's email: pierre.dumont@insa-lyon.fr

Abstract – *TEMPO-oxidised cellulose nanofibril (CNF) hydrogels or cellulose nanocrystal (CNC) hydrogels can now be obtained at high concentrations (> 10 wt.%) and used to fabricate biobased materials and structures. Thus, it is required to control and model their rheology in process-induced multiaxial flow conditions using 3D tensorial models. For that purpose, it is necessary to investigate their elongational rheology. Thus, concentrated TEMPO-oxidised CNF and CNC hydrogels were subjected to monotonic and cyclic lubricated compression tests followed by a relaxation. These tests revealed for the first time that the complex compression rheology of these two electrostatically stabilised hydrogels combines viscoelasticity and viscoplasticity. The effect of their nanofibre content and aspect ratio on their compression response was emphasised and discussed. The ability of a non-linear elasto-viscoplastic model of the literature to reproduce the experiments was also assessed. Even if some discrepancies were observed at low or high strain rates, the model was consistent with the experiments.*

Keywords – cellulose nanofibrils; cellulose nanocrystals; electrostatically stabilised hydrogels; lubricated compression; elongational flow; cyclic tests, elastoviscoplasticity.

1. Introduction

Cellulose nanofibrils (CNFs) and cellulose nanocrystals (CNCs) are the two main categories of nanocellulose produced in the form of colloidal aqueous hydrogels (Dufresne, 2017; De France et al., 2017; Ureña-Benavides et al., 2011; McKee et al., 2014; Abe & Yano, 2011; Abe & Yano, 2012). CNF hydrogels can be produced using various processing routes. These processing routes influence the morphological properties and the physico-chemical surface properties of the nanofibres (Dufresne, 2017; Nechyporchuk, Belgacem, & Bras, 2016; Masruchin et al., 2015) and thus the colloidal stability of the hydrogels. The TEMPO-mediated oxidation pre-treatment process enables obtaining electrostatically stabilised hydrogels at concentrations close to 1 wt.% (Saito et al., 2007; Isogai et al., 2011). Since the last decade, new extraction routes involving the use of twin-screw extruders have been reported to obtain CNF hydrogels with concentrations up to 10 wt.% (Baati et al., 2017; Rol et al., 2017). These hydrogels contain slender nanofibres with a length that is typically comprised between 1000 nm and 2000 nm and a width that ranges from 3 nm to 6 nm (Isogai et al., 2011; Martoïa et al., 2016b). The CNF nanofibres are constituted of both disordered and crystalline regions (Dufresne, 2017; Klemm et al., 2018). CNC hydrogels that are produced via acid hydrolysis of cellulose fibres contain highly crystalline shorter rod-shaped nanofibres with a length that ranges from 100 nm to 200 nm and a width that ranges from 5 nm to 20 nm (Dufresne, 2017; Klemm et al., 2018; Beck-Candanedo et al., 2005) . Recently,

new extraction routes (Reid et al., 2017; Delepierre et al., 2021) have been developed to produce CNCs in the form of powder that can be easily redispersed in water, enabling homogeneous CNC hydrogels with high concentrations up to 25wt.% to be obtained.

The two types of aforementioned hydrogels are promising materials that can be used in a wide range of manufactured biosourced products such as gelling agents for cosmetics (Meftahi et al., 2022), coating slurries for the papermaking industry (Li et al., 2021), thickeners or emulsion stabilisers for the food industry (Gómez H. et al., 2016) or as building blocks to obtain filaments, films or nanopapers as well as foams or aerogels for a wide range of applications (Lundahl et al., 2017; Benítez & Walther, 2017; Gupta et al., 2018; Aulin et al., 2010; Jiang & Hsieh, 2014; Jiang & Hsieh, 2013; Kettunen et al., 2011). During the processing routes involved to transform them, these hydrogels can be subjected to various types of flow conditions, including shear and elongational deformations (Hubbe et al., 2017; Wang et al., 2019). For instance, during the spinning or additive manufacturing of CNF of CNF filaments, these hydrogels can be mainly subjected to shear or elongational flows within the die but also outside the die during the drawing or the deposition of the filaments (Lundahl et al., 2017; Esmaeili et al., 2022; Hausmann et al., 2018). If the shear response of these types of systems at moderate nanofiber contents has been extensively investigated (Hubbe et al., 2017; Martoïa et al., 2015; Nechyporchuk, Belgacem, & Pignon, 2016; Zakani & Grecov, 2020), their elongational response remains largely unexplored. Scarce previous works have reported methodologies based on the principle of capillary flow rheometers equipped with a convergent nozzle (Moberg et al., 2014) or capillary breakup extensional rheometer (Lundahl et al., 2018). However, the interpretation of the acquired experimental data by these setups is complex. More recently, we have proposed to use lubricated compression experiments to study the equi-biaxial flow of concentrated enzymatic CNF hydrogels (Martoïa et al., 2022). This technique enabled revealing that the flow of enzymatic CNF hydrogels was one-phase or two-phase and consolidating, depending on the applied compression strain rate. In the case of one-phase flow conditions, several rheological parameters such as the compression modulus and compression yield stress were measured for concentrated and highly concentrated enzymatic CNF hydrogels (Martoïa et al., 2022). To date, this technique has not been used to investigate the rheology of electrostatically stabilised CNF and CNC hydrogels that are known to exhibit flow properties that are different from flocculated enzymatic CNF hydrogels.

The lack of relevant experimental data on the elongational behaviour of electrostatically stabilised CNF and CNC hydrogels hinders the assessment of existing rheological models (Martoïa et al., 2016a; Bounoua et al., 2016; Fraggedakis et al., 2016) under such flow conditions or the development of more adapted models to describe the three-dimensional flow of these types of hydrogels. Such a lack is even more obvious for concentrated hydrogels, the rheology of which still remains unknown, regardless of the flow conditions.

Thus, to provide a detailed description of the elongational rheology of electrostatically stabilised CNF and CNC hydrogels from moderate to high concentration regimes, we propose to investigate monotonic lubricated compression tests for a wide range of compression strain rates and nanofibre contents. Cyclic compression and relaxation tests were also performed to unveil the viscolelastic and viscoplastic features of these hydrogels. These various experiments enabled a better understanding of the rheology of these hydrogels for various

nanofibre concentrations and aspect ratios. It also enabled assessing the relevance of a non-linear elasto-visco-plastic fluid model from the literature (Saramito, 2009; Fraggedakis et al., 2016).

2. Materials

2.1 Cellulose nanofibrils (CNFs) and cellulose nanocrystals (CNCs)

CNFs were supplied by the Centre Technique du Papier (Grenoble, France) in the form of an aqueous hydrogel at an initial weight (resp. volume) concentration c_0 (resp. ϕ_{f0}) of 1.2 wt.% (resp. 0.8%). This hydrogel was obtained from a bleached kraft wood pulp subjected to a TEMPO-mediated oxidation using a methodology reported by (Saito et al., 2006). Then they were mechanically disintegrated using a homogeniser M-110 EH-30 (GEA Niro Soavi, Parma, Italy). The content of carboxyl groups determined by conductometric titration was 1.5 mmol g^{-1}.

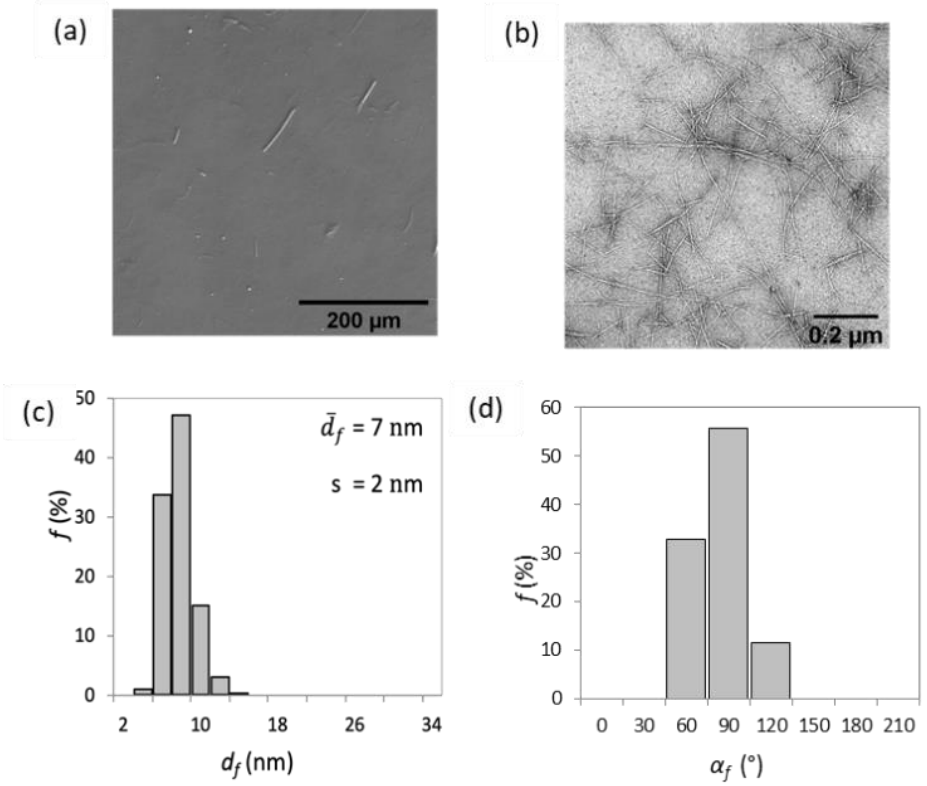

Figure 1*. (a) SEM micrograph of a film obtained after drying a CNF hydrogel diluted at 0.1 wt.%. Images were acquired with a HITACHI S-3500N SEM operating at 15 kV in low vacuum pressure (20 Pa). (b) TEM micrograph of a CNF film obtained after drying a CNF hydrogel diluted at 0.001 wt.%. Films were observed in a Philips CM200 TEM operating at an accelerating voltage of 80 kV. (c) Distribution histogram of the width d_f of CNF nanofibres. (d) Distribution histogram of kink angles α_f of CNF nanofibres (obtained from the manual measurements of 100 nanofibres).*

Figure 1a,b show SEM and TEM micrographs of CNF films that were obtained after drying drops of diluted CNF hydrogels. More details on the methodologies for SEM and TEM image acquisition techniques are reported by Martoïa et al., 2016a.

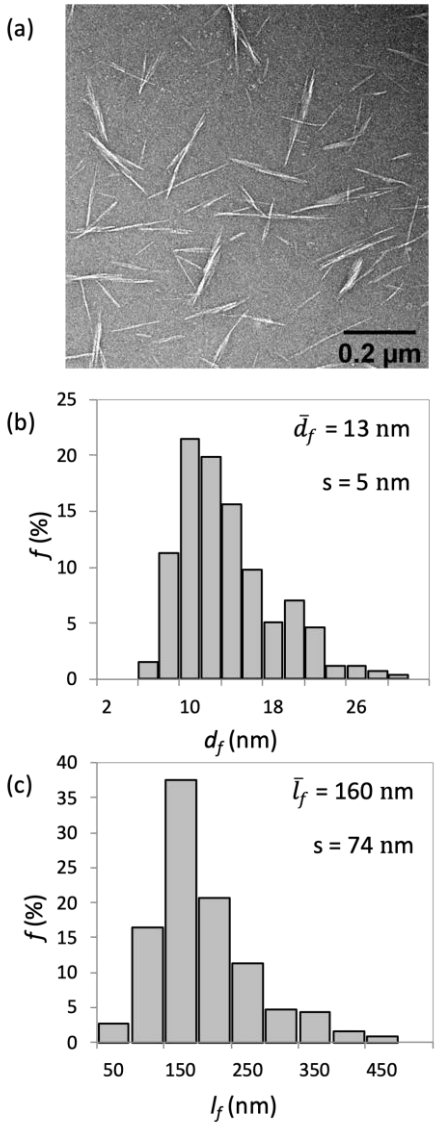

Figure 2. *(a) TEM micrograph of a CNC film obtained after drying a CNC hydrogel diluted at 0.001 wt.%. Films were observed in a Philips CM200 TEM operating at an accelerating voltage of 80 kV. (b) Distribution histogram of the widths d_f of CNCs. (c) Distribution histogram of lengths l_f of CNCs.*

SEM micrographs (Figure 1a) show that the CNF hydrogel contained few microscale elements that corresponded to fibre cell walls fragments that were incompletely fibrillated. A quantitative analysis of these micrographs revealed that these fragments had a mean width of 4 μm and a mean length of 40 µm. In addition, the TEM micrograph (Figure 1b) and the histogram (Figure 1c) show that the CNF hydrogel also contained slender and tortuous nanofibres with a width d_f that ranged between 4 nm and 8 nm with a mean value $\bar{d}_f$ of 7 nm (obtained from the manual measurements of 100 nanofibres), and a mean length $\bar{l}_f$ of 1.2 μm (obtained from 5 manual measurements only), i.e., a high mean aspect ratio $r = \bar{l}_f/\bar{d}_f \approx 176$. Figure 1b also reveals that these nanofibres were tortuous and could be seen as an assembly of straight segments interspersed with kinks (Martoïa et al., 2016a; Martoïa et al., 2016b). The kink angle defined as the misorientation angle between two consecutive segments of an individual nanofibre (Martoïa et al., 2016a; Martoïa et al., 2016b)

exhibited a mean value $\bar{\alpha}_f = 68°$ (Figure 1d). The dimensions of the fragments and nanofibres are in line with the data reported in the literature for similar CNF systems (Martoïa et al., 2016a).

CNCs were supplied by CelluForce (Canada) in the form of spray-dried powder. The content of sulfate ester groups was 0.25 mmol g^{-1}. The TEM micrographs and the histograms shown in Figure 2 reveal that CNCs were rod-shaped nanoparticles with a width d_f that ranged between 8 nm and 14 nm, with a mean width $\bar{d}_f \approx 12.6$ nm (obtained from the manual measurements of 100 CNCs), whereas their length l_f varied from 50 nm to 200 nm, with a mean length $\bar{l}_f \approx 160$ nm (obtained from the manual measurements of 100 CNCs). In comparison with CNFs, CNC particles were much less slender with an aspect ratio r that was close to 12.5, again in line with reported data in the literature (Dufresne, 2017).

2.2 Preparation of concentrated nanocellulose CNF and CNC hydrogels

We have developed a methodology to produce concentrated CNF hydrogels with high weight (resp. volume) concentrations c (resp. ϕ_f) that range from 1.2 wt.% (resp. 0.8%) to 8.6 wt.% (resp. 6%). For each targeted concentration, a mass m of 200 g of CNF hydrogels at the initial concentration c_0 (= 1.2 wt.%) was placed in a vacuum oven (Thermo scientific Heraeus, VT6060M) in a rectangular tray of 250 mL capacity (Grosseron, France) at a vacuum pressure P of 0.01 mbar and a temperature T of 50 °C. The hydrogel was then taken out from the vacuum oven every 20 min and was homogenized with a disperser (IKA Ultra-Turrax T-18) at 3000 rpm. This preparation process was repeated until the target concentration value was reached. Figure 3a-c shows photographs of the as-obtained CNF hydrogels for concentrations 1.2 wt.% to 8.6 wt.%. The concentration of the CNF hydrogels was checked using the gravimetric method (Foster et al., 2018).

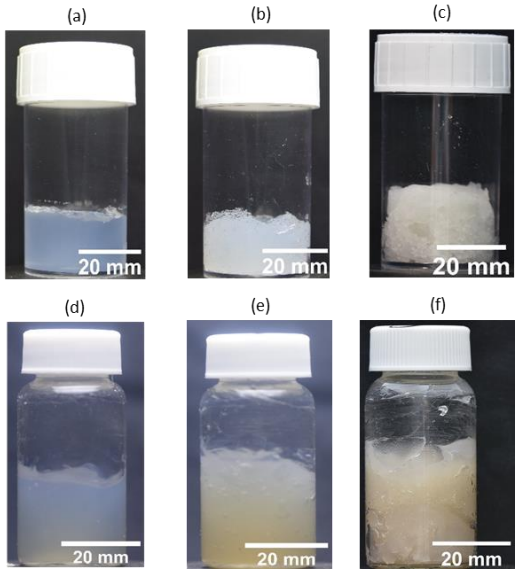

Figure 3. *Photographs showing CNF hydrogels at various weight concentrations c: (a) 1.2 wt.% ($\phi_f = 0.8\%$), (b) 2 wt.% ($\phi_f = 1.4\%$), (c) 8.6 wt.% ($\phi_f = 5.9\%$). Same type of photographs for CNC hydrogels at various weight concentrations c: (d) 6.5 wt.% ($\phi_f = 4.4\%$), (e) 10 wt.% ($\phi_f = 6.9\%$), (f) 24.5 wt.% ($\phi_f = 17.9\%$).*

CNC hydrogels were produced at weight concentrations c (resp. ϕ_f) that ranged from 6.5 wt.% (resp. 4.4%) to 25 wt.% (resp. 17.9%) .The preparation method consisted of slowly adding a known quantity of CNC powder in deionized water while stirring (8000-16000 rpm) using the disperser at 12000 rpm until a homogeneous gel was obtained (Figure 3d-f).

Both CNF and CNC hydrogels had a pH that was comprised between 7 and 7.5. Thus, they could be considered as electrostatically stabilised hydrogels.

Assuming a homogeneous spatial distribution of the centre of mass of the nanofibres as well as a 3D planar random orientation of these nanoparticles in the hydrogels, it is possible to estimate the so-called mean coordination number z, *i.e.*, the average number of contacts between nanofibres, using the statistical tube model (Toll, 1993; Martoïa et al., 2016a) (see SI for the calculation details). For the investigated ranges of concentrations of both CNF and CNC hydrogels, the number z varies between 2.5 (resp. 1.2) and 17 (resp. 5) for CNF (resp. CNC) hydrogels. As $z > 1$ for all concentrations and both hydrogels (Figure S1), this tends to show that the nanofibres form connected networks and that all the studied hydrogels belongs to the concentrated regime (Martoïa et al., 2016a; Balberg et al., 1984).

2.3 Lubricated compression tests

For both CNF and CNC hydrogels, two sets of cylindrical samples with an initial diameter D_0 that was equal to 13.1 mm or 17.5 mm and an initial height $h_0 = 3.0$ mm were prepared and subjected to lubricated compression experiments. To prepare the samples, a weight of 10 g of CNF hydrogel was homogenised at 3000 rpm using the Ultra-Turrax disperser. During shearing, air bubbles were introduced. To remove them, the CNF hydrogel samples were placed in vacuum at 0.01 mbar for a few minutes. A prescribed amount of CNF hydrogel was then poured into a cylindrical mould made from Teflon. Finally, the CNF hydrogel sample was removed carefully from the mould.

Two types of simple lubricated compression tests were performed: monotonic (Figure 4a), possibly followed by stress relaxation, and cyclic load-unload (Figure 4b) tests. The experiments were performed with parallel plates (25-mm width) mounted on a universal tension-compression testing machine (Shimadzu – AG-X) equipped with a force sensor of 100 N. Teflon sheets were stuck to the surface of these plates (Martoïa et al., 2022). In addition, to avoid friction-induced forces, the plates were coated with silicone oil with a shear viscosity $\mu = 0.02$ Pa s (Chalencon et al 2010, Martoia et al 2022). During these tests, the instantaneous height h of the samples, compression force F and time t were recorded. For both CNF and CNC hydrogels, the monotonic compression experiments were carried out with constant compression velocities $\dot{h}$ that ranged from 0.2 mm min^{-1} to $150\ \text{mm min}^{-1}$. These velocities correspond to initial strain rates $\dot{\varepsilon}_0 = |\dot{h}/h_0|$ that ranged between $0.001\ \text{s}^{-1}$ and $0.8\ \text{s}^{-1}$. By assuming the hydrogel incompressibility, the axial compression stress $\sigma = 4|F|h/(\pi h_0 D_0^2)$ was plotted as a function of the axial compression strain $\varepsilon = |\ln(h/h_0)|$ (up to a maximum strain $\varepsilon = 0.9$). As illustrated in Figure 4a, the compression modulus E of the CNF and CNC hydrogels was measured from the linear part of the monotonic stress-strain curves in a strain range $0.02 \leq \varepsilon \leq 0.1$. Flow stresses denoted $\sigma_{0.8}$ were measured at a strain $\varepsilon = 0.8$. In addition, to investigate relaxation effects, for some of these experiments, the evolution of the compression stress σ was measured as a function of time t for 100 s after reaching the maximum compression strain. Cyclic

lubricated compression tests (Figure 4b) that consisted of three successive load-unload cycles were performed at an initial strain rate $\dot{\varepsilon}_0 = 0.0027\ s^{-1}$ with increasing the axial compression strain ε. The strain recovery ratio of the first load-unload cycle was denoted $\Delta\varepsilon_e/\varepsilon_c$ where $\Delta\varepsilon_e$ was the recovery strain amplitude of the first cycle (Figure 4b) and ε_c the maximum strain attained prior to unloading. During the tests, side views of the deformed samples were also acquired using a high-frequency camera.

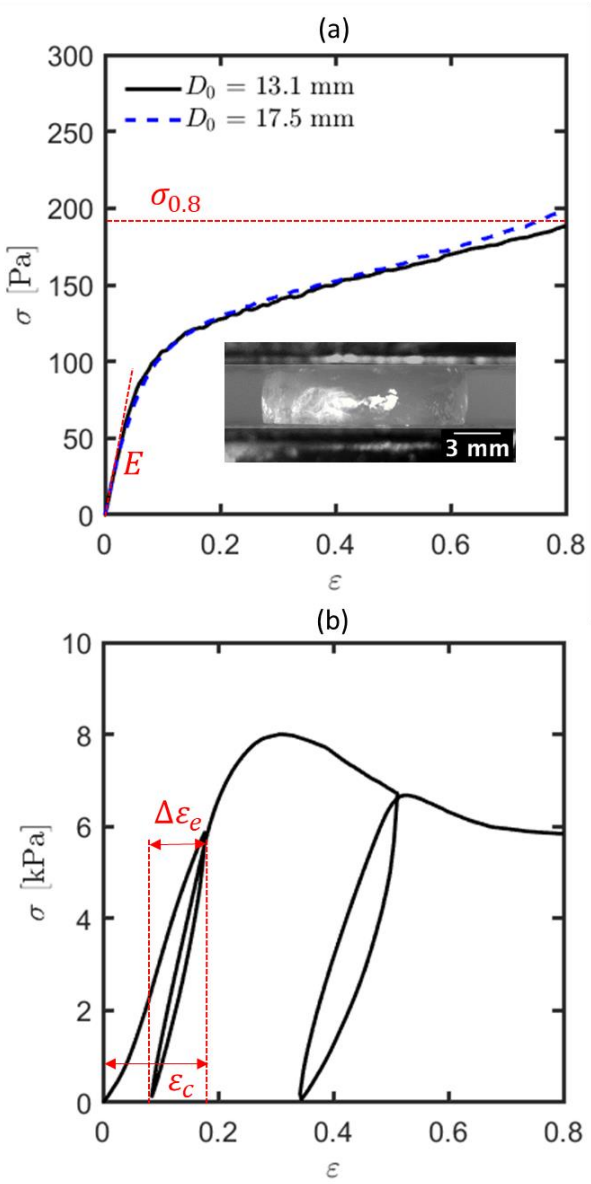

Figure 4*. (a) Typical stress-strain curves obtained during monotonic compression of a CNC hydrogel ($\phi_f = 5.1$ %) at an initial strain rate $\dot{\varepsilon}_0 = 0.05\ s^{-1}$ and two initial sample diameters D_0 = 13.1 mm and 17.5 mm (the inset photographs show the compression device used to perform the lubricated compression tests on cylindrical samples). (b) Typical compression stress-strain curve obtained during load-unload-sequences of a CNF hydrogel ($\phi_f = 5.9\%$).*

Following the methodology reported in several studies (Guiraud et al., 2012; Guiraud et al., 2013; Orgéas et al., 2008), the efficiency of the lubrication was investigated by performing several preliminary monotonic compression experiments with CNF and CNC samples having

different diameters, *i.e.*, $D_0 \approx 13.1$ mm and 17.5 mm. As an example, Figure 4a shows that the compression response did not significantly vary with the sample diameters (here in the case of CNC hydrogels) which proved that friction effects could be neglected. Photographs of the hydrogel samples acquired during their compression also reinforced this assumption since they proved that samples deformed as plug flows along the entire compression strain range. Similar results were obtained for CNF hydrogels. Consequently, all of the experiments used to present and to discuss results in the next section were carried out with samples with a diameter $D_0 = 13.1$ mm.

3. Results and discussion

3.1 Effects of the compression strain and strain rate

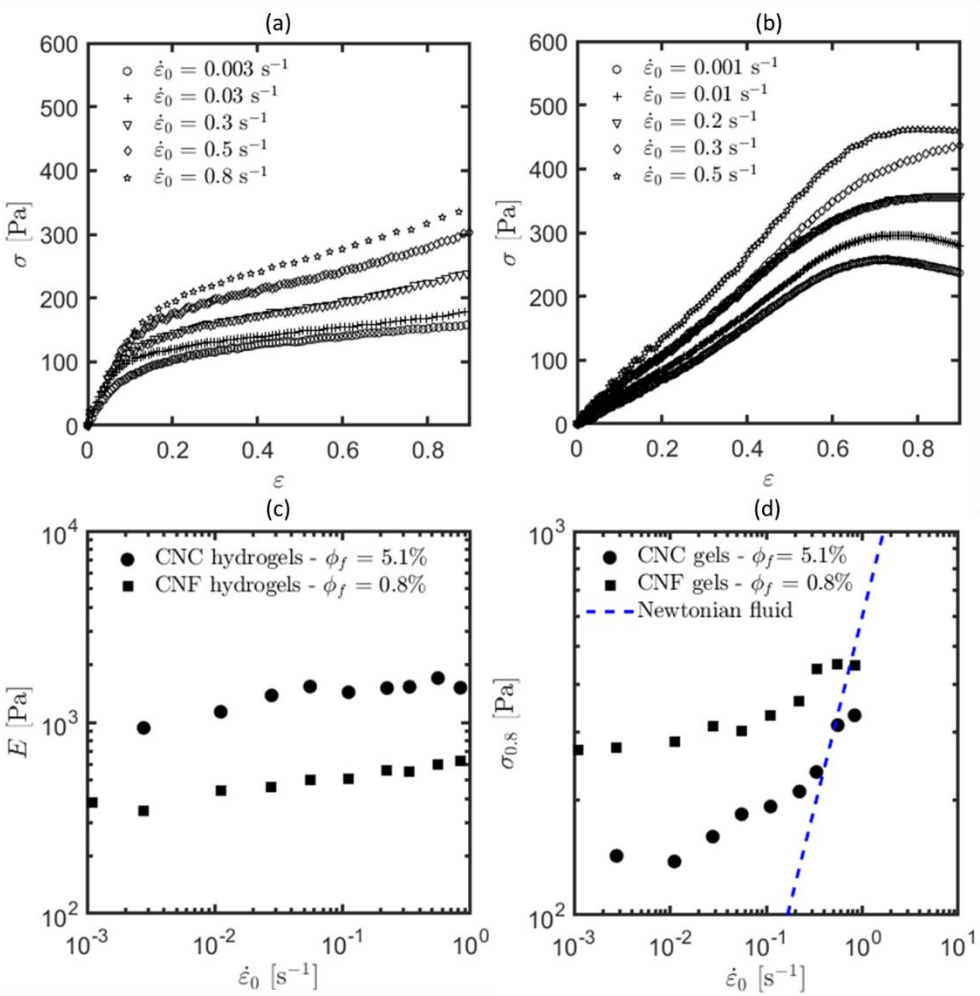

4.

5. ***Figure 5***. *Monotonic stress-strain curves obtained at various initial compression strain rates* $\dot{\varepsilon}_0$ *of (a) CNC hydrogels at* $\phi_f = 5.1\%$ *and (b) CNF hydrogel at* $\phi_f = 0.8\%$. *(c) Evolution of the compression modulus* E *of CNC (resp. CNF) hydrogels at* $\phi_f = 5.1\%$ *(resp.* $\phi_f = 0.8\%$*) as a function of the initial strain rate* $\dot{\varepsilon}_0$. *(d) Evolution of the stress* $\sigma_{0.8}$ *as a function of the the initial strain rate* $\dot{\varepsilon}_0$ *for the same hydrogels. For comparison purpose with CNC and CNF hydrogels, the continuous line shows the response of a Newtonian fluid with an elongational viscosity of 600 Pa s, respectively. In graphs c and d, the symbols represent the mean values of the parameters obtained from three measurements for each testing condition.*

The graphs of Figure 5 show the compression responses of both CNC and CNF hydrogels for nanofibre volume contents ϕ_f = 5.1% and 0.8%, respectively at various strain rates. For these moderate contents, both types of hydrogels exhibited a quite different compression behaviour. For CNC hydrogels (Figure 5a), a quasi-linear increase of the compression stress σ with the compression strain ε was observed up to a compression strain of approximately 0.15, regardless of the initial compression strain rate $\dot{\varepsilon}_0$. Then, a non-linear transition occurred and eventually the compression stresses exhibited a slight strain hardening up to the maximum compression strain $\varepsilon \approx 0.9$. The hardening was all the more pronounced as the initial compression strain rate $\dot{\varepsilon}_0$ was increased. For CNF hydrogels, Figure 5b shows that the stress σ exhibited a sharp and quasi-linear increase with increasing the compression strain ε, but this regime reached values as large as approx. 0.5. The stress then reached a plateau or a maximum value and eventually showed a progressive decrease for strains higher than approx. 0.65. Such a softening behaviour was observed for the lowest studied CNF contents, i.e., ϕ_f = 0.8% and 1.4%, regardless of the initial strain rate $\dot{\varepsilon}_0$. On the contrary, for the other investigated CNF contents, i.e., ϕ_f = 2.8%, 4.3% and 5.9%, the initial sharp increase of the compression curves and the transition towards a softening flow mode occurred for maximum strains ε that were only equal to 0.15-0.25 (Figure 6a,b).

Figure 5c shows that the compression modulus E for CNC and CNF hydrogels slightly increased with increasing the initial strain rate $\dot{\varepsilon}_0$, highlighting possible viscoelastic effects. Figure 5d shows that the stress $\sigma_{0.8}$ is practically constant within a strain rate range $10^{-3} \leq \dot{\varepsilon}_0 \leq 10^{-1}$ s^{-1}. This tends to show these hydrogels exhibited strain rate independent plasticity with the presence of a yield stress at low strain rates. The stress $\sigma_{0.8}$ also showed a non-linear pronounced increase for initial strain rates $\dot{\varepsilon}_0 > 10^{-1}$ s^{-1}. The comparison of the experimental trends obtained for CNC and CNF hydrogels with the continuous line (i.e., response of a Newtonian fluid under lubricated compression) shown in Figure 5d tends to show that these materials exhibited a thinning behaviour.

5.1 Effect of the nanofibre content ϕ_f

The compression stress-strain curves shown in Figure 6a,b reveal the great increase of stress levels with increasing the nanofibre content ϕ_f, whatever the considered hydrogel. Interestingly, the flow stresses were of the same order of magnitude for both hydrogels in spite of the quite large differences in the nanofibre content. For instance, the flow stress measured for a CNC 14.1%-content is close to the flow stress measured for a CNF 4.3%-content. As suggested in Martoïa et al., 2016a, this trend can be related to the large difference in the aspect ratios r of these two types of nanofibres: at given nanofibre content, the nanofibre connectivity in CNF hydrogels (r = 171) is expected to be much higher compared to that of the CNC hydrogels (r = 12.5), and so the stress levels recorded upon compression.

It is interesting to notice that Figure 6c reveals that the evolution of the normalised compression modulus $E/E_{\phi_f=0.04}$ of the two type of hydrogels followed the same increasing power-law with the nanofibre content ϕ_f, thereby revealing that similar deformation mechanisms could occur at nanofibre scale and at low strains. As observed from the previous TEM micrographs, CNF nanofibres could be seen as an assembly of rod-like segments with a length of a hundred nanometers interspersed by kinks. From this viewpoint, CNC and

CNF hydrogels could possibly be considered to form networks of rod-like particles with quite similar microstructures.

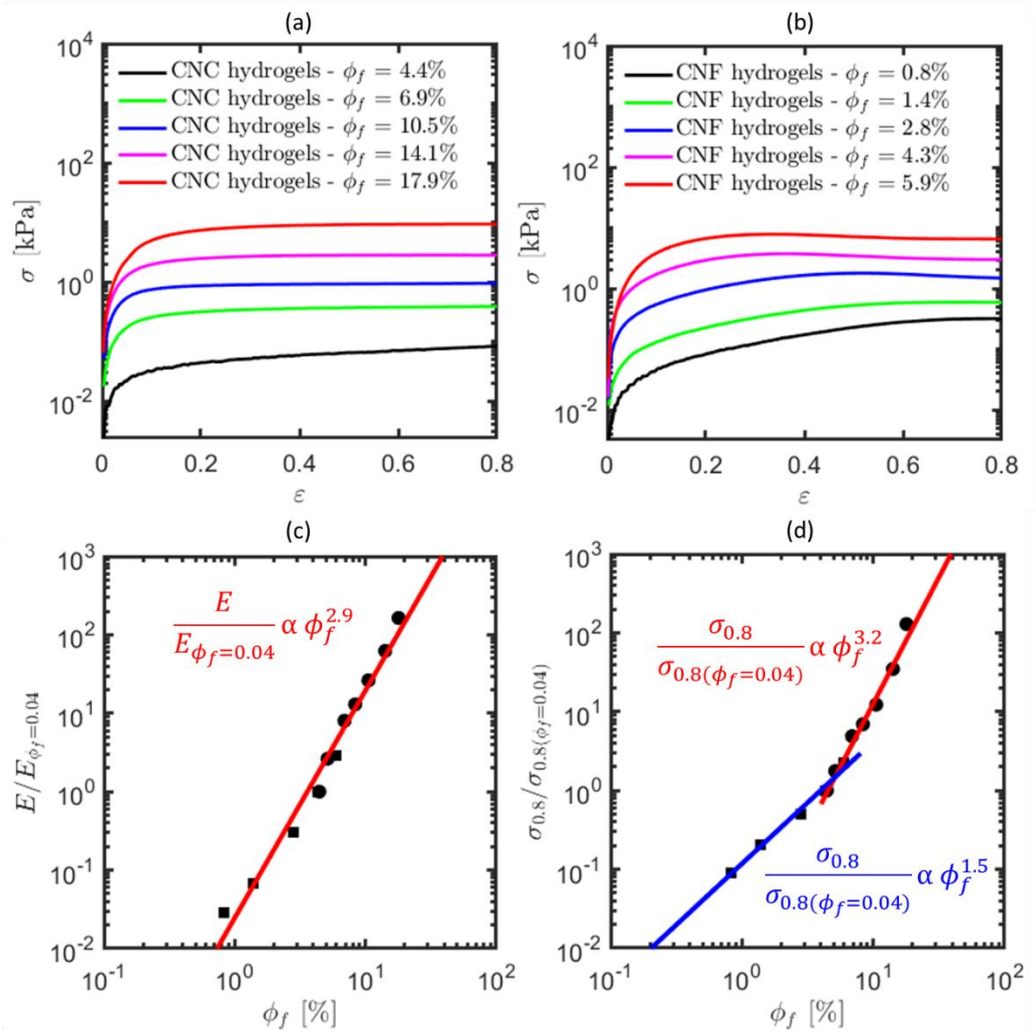

Figure 6*. Compression stress-strain curves obtained for CNC (a) and CNF (b) hydrogels with various nanofibre contents* ϕ_f *at an initial axial strain rate* $\dot{\varepsilon}_0 = 10^{-2}$ *s*$^{-1}$*. (c) Evolution of the normalised compression modulus* $E/E_{\phi_f=0.04}$ *(c) and the normalised stress* $\sigma_{0.8}/\sigma_{0.8(\phi_f=0.04)}$ *(d) with the nanofibre content* ϕ_f *for CNC and CNF hydrogels (initial strain rate* $\dot{\varepsilon}_0 = 10^{-2}$ *s*$^{-1}$*).*

For the flow stresses, the situation was more contrasted as Figure 6d shows that the normalised stress $\sigma_{0.8}/\sigma_{0.8(\phi_f=0.04)}$ did not follow the same scaling laws for the two types of hydrogels. Figure S2 (SI) also shows the crucial role of the nanofibre entanglement characterised through the mean coordination number z on the rheological behaviour of both hydrogels. However, the curves shown in Figure S2 for CNF hydrogels and CNC hydrogels did not superimpose. This tends to show that the entanglement alone cannot explain the non-linear increase of the flow stress with the concentration. Other parameters that are related to the colloidal interactions that arise between the nanofibres might have an effect on the rheology of the hydrogels. For instance, as discussed in Figure 7 in Martoïa et al., 2016a, the colloidal forces depend non-linearly on the concentration ϕ_f and the nanofibre orientation. It is also possible that CNC self-organised domains or CNF aggregates form in

these concentrated hydrogel microstructures. The deformation mechanisms of these domains or aggregate could also be at the origin of the complex evolution of the flow stress observed in Figure 6d.

In addition, Figure S3 in Supplementary Information shows the evolution of a compression yield stress estimated from shear experiments reported by Martoïa et al., 2016a using a Von Mises criterion (Martoïa et al., 2022) for TEMPO-oxidised CNF hydrogels with low to moderate concentrations ($0.1\ \% \leq \phi_f \leq 0.7\ \%$) with the evolution of the flow stress $\sigma_{0.8}$ measured in this study for low strain rates. This graphs shows that the data obtained for similar nanofibre contents ϕ_f, i.e., 0.7 % for Martoïa et al., 2016a and 0.8% for the present study, were of the same order of magnitude. However, the power-law evolution of the flow stress measured at low strain rates was different in both studies. The power-law exponent for the evolution of the flow stress $\sigma_{0.8}$ of the CNF hydrogels with ϕ_f was equal to 1.5 for this study, whereas it was close to 3 in the study from Martoïa et al., 2016a. This difference suggests that other types of deformation mechanisms or microstructure evolution occurred, possibly resulting from the difference in the test kinematics (shear vs. compression).

5.2 Analysis of cyclic compression tests coupled with optical observations

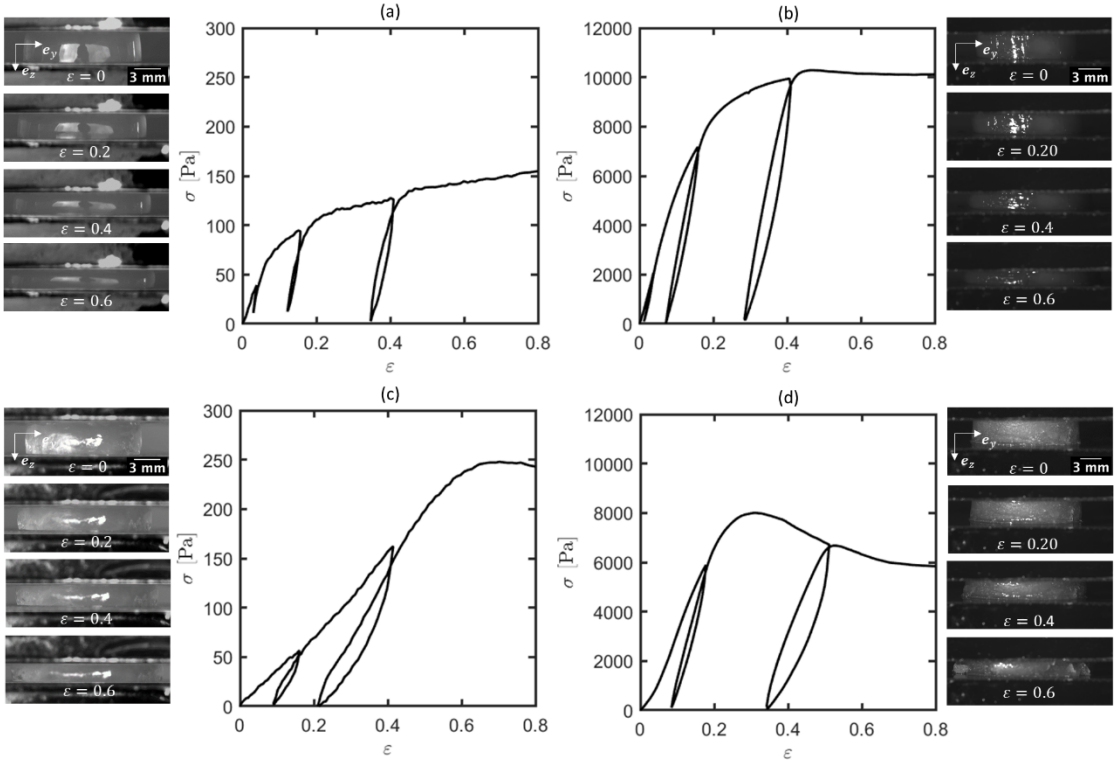

Figure 7*. (a,b) Stress-strain curves obtained during the load-unload cyclic compression tests of a CNC hydrogel with* $\phi_f = 5.1\%$ *(a) and* $\phi_f = 17.9\%$ *(b) for an initial strain rate* $\dot{\varepsilon}_0 = 3 \times 10^{-2}$ *s*$^{-1}$*. (c,d) Same type of curves for a CNF hydrogel with* $\phi_f = 0.8\%$ *(c) and* $\phi_f = 5.9\%$ *(d) for an initial strain rate* $\dot{\varepsilon}_0 = 3 \times 10^{-2}$ *s*$^{-1}$*. The photographs show the evolution of the geometry of the corresponding hydrogel samples at various strains* ε*.*

The following results further emphasise the complex and non-linear rheology of both type of hydrogels, with viscoelastic and plastic effects. Hence, the graphs in Figure 7 show the response of CNC and CNF hydrogels at moderate and high nanofibre contents under

load-unload compression cycles. It is worth noticing that after unloading and reloading up to the load reversion point ε_c, the compression curves practically recovered the stress path it had before the load reversion (Figure 6). These tests also revealed that the elastic strain recovery $\Delta\varepsilon_e$ upon unloading was not complete, whatever the considered reversion strain ε_c. This was quantified in the quasi-linear regime by calculating the elastic strain recovery ratio $\Delta\varepsilon_e/\varepsilon_c$ shown in Figure 8. As evidenced from this figure, the strains measured after unloading for each cycle could result from a possible plastic behaviour of both tested hydrogels. This would have to be confirmed by performing strain recovery tests. Besides, the ratio $\Delta\varepsilon_e/\varepsilon_c$ increased both for CNF and CNC hydrogels with the nanofibre content (except for CNC hydrogels with $\phi_f > 0.10$ where it slightly decreased), emphasising the increasing role of the elastic deformation of the nanofibre network with ϕ_f. Conversely, it is interesting to note that the elastic recovery ratio is close to zero for the lowest nanofibre contents for the CNC hydrogels: for such low nanofibre content, the elastic deformation of the nanofibre network was possibly restrained and only viscoplastic micromechanisms would be prone to occur (nanofibre-nanofibre contacts and nanofibre-water interactions). A possible origin for the slight decrease of the ratio $\Delta\varepsilon_e/\varepsilon_c$ for CNC hydrogels could also be related the formation of self-organised domains (Ureña-Benavides et al., 2011; Shafeiei-Sabet et al., 2013) or agglomerates (Zakani & Grecov, 2022) within these hydrogels with poor cohesive properties at the junctions between these blocks.

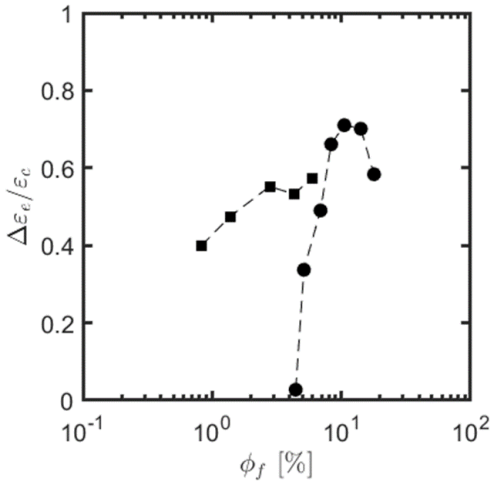

Figure 8*. Evolution of the strain recovery ratio $\Delta\varepsilon_e/\varepsilon_c$ for CNC (circular symbols) and CNF (square symbols) hydrogels as a function of the volume fraction ϕ_f.*

In addition, this graph also reveals that the CNF hydrogels exhibited higher elastic strain recovery ratios compared to the CNC hydrogels for comparable nanofiber contents ϕ_f. This could be again related to the higher aspect ratio of CNF nanofibres compared to that of CNC nanofibres, which leads to higher nanofibre connectivity in CNF hydrogels (Martoïa et al., 2016a).

Upon reloading, it was observed that the stress-strain path was different from unloading, confirming again the viscoelastic properties of both types of hydrogels. This is also in line with the stress relaxation observed in Figure 9f and Figure 10f for both CNC and CNF hydrogels, after stopping the sample loading. Lastly, the inset photographs of Figure 7 did not reveal any obvious evolution of the integrity of the CNC samples. On the contrary, for CNF hydrogels, scattered radial cracks could be observed on the periphery of the samples

for the highest compression strains $\varepsilon \geq 0.4$. These damage mechanisms could also be a possible origin of the plastic deformation upon unloading for large strains and the softening of stresses in this large strain range.

6. An elasto-viscoplastic model to reproduce experimental trends

6.1 Principle

We propose to use a literature tensorial model in order to predict the experimental results described in the previous section, with the following typical rheological features:

- A partial elastic recovery during load-unload cyclic experiments at various compression strains ε, suggesting the presence of a compression yield stress σ_y
- A progressive and uncomplete relaxation of the compression stress σ during relaxation tests,
- A quasi-linear response of the compression stress σ with the compression strain ε at low compression strains ε,
- A poor sensitivity of the flow stress $\sigma_{0.8}$ with the compression strain rate $\dot{\varepsilon}$ at low compression strain rates, reinforcing the assumption stated in the first point above,
- A non-linear evolution of the flow stress $\sigma_{0.8}$ with the compression strain rates $\dot{\varepsilon}$ for the highest values of the compression strain-rates, suggesting the presence of a thinning behaviour.

In light of these observations, we checked whether the phenomenological tensorial model proposed by Saramito5(2009) to describe the three-dimensional behaviour of elasto-visco-plastic (EVP) fluids was capable to mimic the compression data gathered for CNC and CNF hydrogels. This EVP model combines both the Oldroyd viscoelastic model (Saramito, 2007) and the Herschel-Bulkley viscoplastic model (Saramito, 2009; Fraggedakis et al., 2016). Thus, below the yield stress of the hydrogel, this one behaves as a viscoelastic solid, whereas above a yield stress, it behaves as a non-linear viscoelastoplastic fluid. Hence, the compression stress σ of an EVP fluid (seen as an isotropic incompressible fluid) subjected to a compression strain-rate $\dot{\varepsilon}$ along $\mathbf{e}_z$ is obtained by solving numerically the following set of differential equations:

$$\left\{\begin{array}{c} \sigma = \tau_{zz} - \tau_{yy} + 3\eta\dot{\varepsilon} \\ \frac{3}{E}\frac{\partial \tau_{zz}}{\partial t} - \frac{6a\dot{\varepsilon}}{E}\tau_{zz} + \max\left(0, \frac{|\tau_d| - \sigma_y/\sqrt{3}}{k|\tau_d|^n}\right)^{\frac{1}{n}} \tau_{zz} = 2\dot{\varepsilon} \\ \frac{3}{E}\frac{\partial \tau_{yy}}{\partial t} + \frac{3a\dot{\varepsilon}}{E}\tau_{yy} + \max\left(0, \frac{|\tau_d| - \sigma_y/\sqrt{3}}{k|\tau_d|^n}\right)^{\frac{1}{n}} \tau_{yy} = -\dot{\varepsilon} \\ |\tau_d| = \sqrt{\frac{{\tau_{zz}}^2 + {\tau_{yy}}^2 - 2\tau_{zz}\tau_{yy}}{3}} \end{array}\right\} \quad \text{Equation 1}$$

where η is the shear viscosity, k the consistency, n the strain-rate sensitivity index, E the compression modulus, and σ_y the compression yield stress of the EVP fluid. The parameter $a \in [-1, 1]$ is associated to the Gordon-Schowalter's material derivative where $a = 0$

corresponds to the Jaumann derivative while $a = 1$ and $a = -1$ are associated to the upper and the lower convected derivatives, respectively (Saramito, 2009; Saramito, 2007). This parameter was set it to 0 to cancel non-physical effects induced by the second terms of the left hand side of the second and third equations listed in Equation 1. Lastly, the stresses τ_{zz} and τ_{yy} are the longitudinal and transverse components of the extra stress tensor of the EVP fluid.

6.2 Comparison of the model predictions with the experiments

Figure 9 and Figure 10 show the model predictions and also its limitations for both CNC and CNF hydrogels, respectively. The model was computed by finding a best possible adjustment of its parameters to fit the experimental data. In addition, the axial strain rate $\dot{\varepsilon}$ was calculated using a constant compression plate velocity, resulting in an evolution with the compression strain ε that is shown in the inset of Figure 9a.

Table 1. Parameters of the EVP model used to best reproduce the compression behaviour of CNC ($\phi_f = 5.1\%$) and CNF hydrogels ($\phi_f = 0.8\%$)

	E [Pa]	σ_y [Pa]	k [Pa s^n]	n	η [Pa s]
CNC hydrogel	1000	100	25	0.5	30
CNF hydrogel	400	250	150	0.6	35

For CNC hydrogels, the model predictions were in line with the experimental trends except at the lowest strain rates (Figure 9a,b) where the strain hardening of stress was not correctly reproduced. This strain hardening possibly results from the complex evolution of the structure of the CNC hydrogels such as flow-induced CNC orientation or formation of self-organised (nematic) domains (Esmaeili et al., 2022; Zakani & Grecov, 2022). Consequently, the evolution of the flow stress $\sigma_{0.8}$ with $\dot{\varepsilon}_0$ was underestimated as shown in Figure 9e. The strain relaxation experiment (Figure 9f) revealed another limitation of the model. If the model could predict an uncomplete relaxation of the CNC hydrogel, this relaxation was less pronounced than in the experiments. This could be improved, e.g. by adding to the overall model other Oldroyd elements with other relaxation times.

For CNF hydrogels, the model predictions showed a rather good agreement with the experiments at low strain rates. On the contrary, the model could not reproduce neither the stress hardening of the quasi-linear regime nor the position of the stress plateau for the largest strain rates (Figure 10c,d). The model does not account for any nanofibre flow-induced orientation that could be at the origin of the hardening stresses nor damage phenomena such as cracks that were observed for CNF hydrogels at the largest strains. This would require to modify and couple the model with equations including variables that would describe the flow-induced structure evolution of the hydrogels. Regarding the relaxation experiments, a similar limitation of the model was observed as for CNC hydrogels.

It should be also noticed that the model behaves as an elastic solid at the lowest strains. Thus, it is not able to reproduce the partial elastic strain recovery that was observed in Figure 7 for both hydrogels.

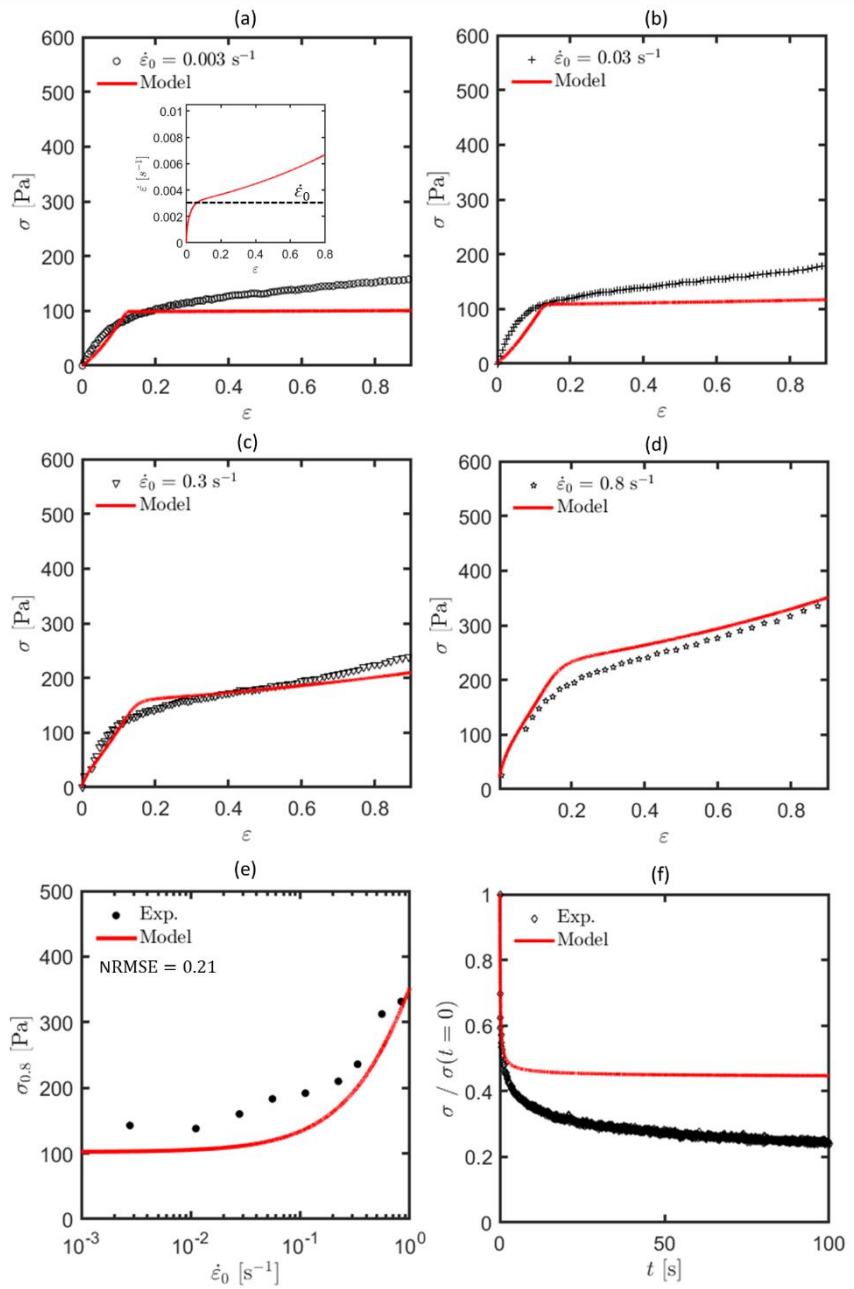

Figure 9. *(a-d) Stress-strain curves obtained for CNC hydrogels (ϕ_f = 5.1%) at various initial compression strain rates $\dot{\varepsilon}_0$. The model predictions are the red curves whereas experimental curves appear in black. The inset graph in Figure 9a shows the evolution of the strain rate $\dot{\varepsilon}$ during compression used to compute the model. (e) Experimental results (symbols) and model prediction (red curve) for the evolution of the flow stress $\sigma_{0.8}$ with the compression strain rate $\dot{\varepsilon}_0$ of a CNC hydrogel with ϕ_f = 5.1%. (f) Experimental results (symbols) and model predictions (red curve) for the time-evolution of $\sigma(t)/\sigma(t=0)$ of a CNC hydrogel (ϕ_f = 5.1%) during a relaxation experiment performed after a monotonic simple compression up to $\varepsilon = 0.96$ with an initial compression strain rate $\dot{\varepsilon}_0$ = 0.3 s^{-1}. NRMSE: normalised root-mean-square error.*

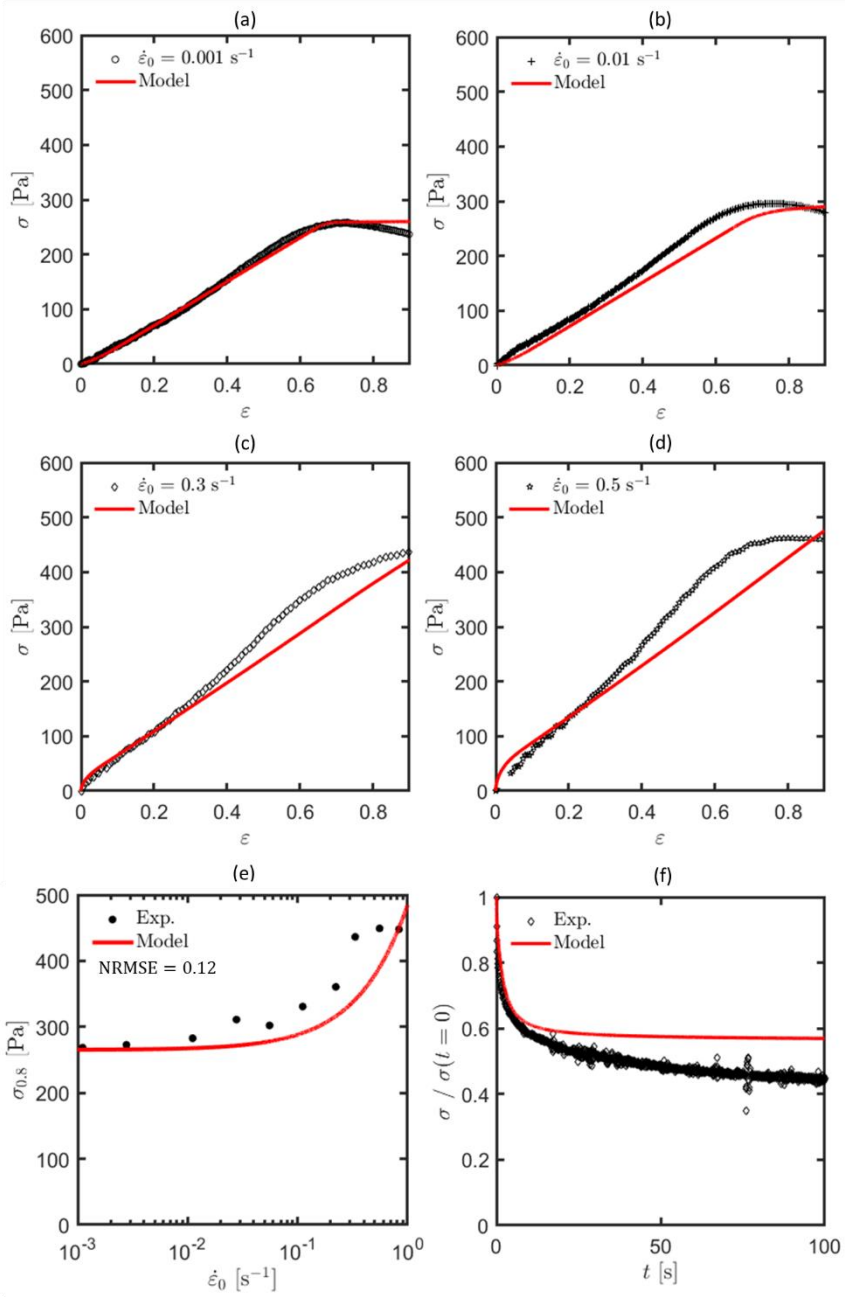

Figure 10*. (a-d) Stress-strain curves obtained for CNF hydrogels (ϕ_f = 0.8%) at various initial compression strain rates $\dot{\varepsilon}_0$. The model predictions are the red curves, whereas experimental curves appear in black. (e) Experimental results (symbols) and model prediction (red curve) for the evolution of the flow stress $\sigma_{0.8}$ with the compression strain rate $\dot{\varepsilon}_0$ of a CNC hydrogel with ϕ_f =0.8%. (f) Experimental results (symbols) and model predictions (red curve) for the time-evolution of $\sigma(t)/\sigma(t=0)$ of a CNC hydrogel (ϕ_f= 0.8%) during a relaxation experiment performed after a monotonic simple compression up to $\varepsilon = 0.96$ with an initial strain rate $\dot{\varepsilon}_0$ = 0.3 s^{-1}. NRMSE: normalised root-mean-square error.*

7. Conclusion

In this study, we prepared various CNC and CNF hydrogels with moderate to concentrated nanofibre contents. Their elongational behaviour was investigated using lubricated compression with different loading conditions: monotonic or cyclic strain-controlled compression loadings as well as stress relaxation after monotonic compression. Besides, the compression device was equipped with an optical visualisation system, enabling the homogeneity of the flow conditions and the sample deformation mechanisms to be assessed.

Both types of hydrogels exhibited two flow regimes. First, a quasi-linear regime occurred in a larger strain range for the CNF hydrogels than for the CNC hydrogels. This regime was followed by the occurrence of a stress transition leading to a plateau or a stress softening for CNF hydrogels, or a stress hardening for CNC hydrogels. We also showed that the strain rate and the hydrogels nanofibre content had an effect on the compression response and affected several properties such as the compression modulus and the flow stress. The compression modulus was shown to slightly increase with increasing the strain rate, whereas the flow stress followed a non-linear evolution that was similar to that of yield stress fluids with thinning effects at high strain rates. We also observed that the compression modulus and the flow stress were power-law functions of the nanofibre content. Similar power-law exponents were found for the compression modulus of both types of systems, suggesting that similar underlying deformation mechanisms occurred at low strains. On the contrary, the power-law exponent describing the evolution of the flow stress with the nanofibre content were different for CNC and CNF hydrogels, suggesting that the flow mechanisms at larger strains were different.

Load-unload cycling tests revealed a partial elastic strain recovery was recorded even in the quasi-linear regime, regardless of the type of hydrogels. The higher the nanofibre content, the higher the elastic recovery. This tends to show that a plastic strain arose after unloading, a scenario that would have to be confirmed by recovery experiments. The analysis of all the results gathered for both hydrogels revealed that these materials exhibited a complex rheological behaviour that combined typical features of visco-elasto-plastic fluids or solids. In light of these observations, their compression responses were compared to those of the predictions of a non-linear elasto-visco-plastic model (Saramito, 2009). The model is able to capture the behaviour of the hydrogels for different situations. However, typically some discrepancies were observed at low or high strain rates, depending on the nature of the hydrogels. To improve the model, several modifications should be done to the model to better represent the flow-induced phenomena. To represent possible phenomena such as the evolution of the CNC or CNF orientation, CNF conformation, or nematic effects in CNC hydrogels, it would be necessary to integrate structural descriptors in the model and to couple it with evolution equations for these descriptors (Esmaeili et al., 2022; Hausmann et al., 2018).

Besides, the CNF hydrogels were shown to exhibit damage for the highest compression strains. Representing this behaviour would also require to develop more advanced models, possibly by including variables representing the failure (Keshavarz et al., 2017) or the damage evolution.

From an experimental viewpoint, the original compression methodology that was reported in this study was shown to be efficient to investigate the elongational flow properties of nanocellulose hydrogels with substantial nanofibre contents. The knowledge of the elongational behaviour of these hydrogels is crucial to understand and model the phenomena that occur for instance during the drawing or their deposition in the form of filaments in additive manufacturing or spinning processes (Lundahl et al., 2017; Esmaeili et al., 2022 ; Hausmann et al., 2018). However, the experimental setup could be improved to perform compression experiments at larger strain rates. From a modelling viewpoint, the validity of the model should be assessed at higher strain rates and for other types of flow kinematics.

Acknowledgments

This research was supported by IDEX Université Grenoble Alpes and Labex Tec21. The authors gratefully acknowledge LabEX Tec 21 and the research site of INSA Lyon at Oyonnax for administrative and technical support. The laboratories 3SR is part of the LabEx Tec 21 (Investissements d'Avenir-grant agreement n ◦ ANR-11-LABX-0030) and the Carnot Institute Polynat (n ◦ ANR16-CARN-0025). The authors also thank J.-L. Putaux (CERMAV) for his support in the experiments performed using the transmission electron microscope.

References

Abe, K., & Yano, H. (2011). Formation of hydrogels from cellulose nanofibers. *Carbohydrate Polymers*, *85*(4), 733–737. https://doi.org/10.1016/j.carbpol.2011.03.028

Abe, K., & Yano, H. (2012). Cellulose nanofiber-based hydrogels with high mechanical strength. *Cellulose*, *19*(6), 1907–1912. https://doi.org/10.1007/s10570-012-9784-3

Aulin, C., Netrval, J., Wågberg, L., & Lindström, T. (2010). Aerogels from nanofibrillated cellulose with tunable oleophobicity. *Soft Matter*, *6*(14), 3298–3305. https://doi.org/10.1039/C001939A

Baati, R., Magnin, A., & Boufi, S. (2017). High Solid Content Production of Nanofibrillar Cellulose via Continuous Extrusion. *ACS Sustainable Chemistry & Engineering*, *5*(3), 2350–2359. https://doi.org/10.1021/acssuschemeng.6b02673

Balberg, I., Anderson, C. H., Alexander, S., & Wagner, N. (1984). Excluded volume and its relation to the onset of percolation. *Physical Review B*, *30*(7), 3933–3943. https://doi.org/10.1103/PhysRevB.30.3933

Beck-Candanedo, S., Roman, M., & Gray, D. G. (2005). Effect of Reaction Conditions on the Properties and Behavior of Wood Cellulose Nanocrystal Suspensions. *Biomacromolecules*, *6*(2), 1048–1054. https://doi.org/10.1021/bm049300p

Benítez, A. J., & Walther, A. (2017). Cellulose nanofibril nanopapers and bioinspired nanocomposites: A review to understand the mechanical property space. *Journal of Materials Chemistry A*, *5*(31), 16003–16024. https://doi.org/10.1039/C7TA02006F

Bounoua, S., Lemaire, E., Férec, J., Ausias, G., & Kuzhir, P. (2016). Shear-thinning in concentrated rigid fiber suspensions: Aggregation induced by adhesive interactions. *Journal of Rheology*, *60*(6), 1279–1300. https://doi.org/10.1122/1.4965431

De France, K. J., Hoare, T., & Cranston, E. D. (2017). Review of Hydrogels and Aerogels Containing Nanocellulose. *Chemistry of Materials*, *29*(11), 4609–4631. https://doi.org/10.1021/acs.chemmater.7b00531

Delepierre, G., Vanderfleet, O. M., Niinivaara, E., Zakani, B., & Cranston, E. D. (2021). Benchmarking Cellulose Nanocrystals Part II: New Industrially Produced Materials. *Langmuir*, *37*(28), 8393–8409. https://doi.org/10.1021/acs.langmuir.1c00550

Dufresne, A. (2017). *Nanocellulose: From Nature to High Performance Tailored Materials*. Walter de Gruyter GmbH & Co KG.

Esmaeili, M., George, K., Rezvan, G., Taheri-Qazvini, N., Zhang, R., & Sadati, M. (2022). Capillary Flow Characterizations of Chiral Nematic Cellulose Nanocrystal Suspensions. *Langmuir*, *38*(7), 2192–2204. https://doi.org/10.1021/acs.langmuir.1c01881

Foster, E. J., Moon, R. J., Agarwal, U. P., Bortner, M. J., Bras, J., Camarero-Espinosa, S., Chan, K. J., Clift, M. J. D., Cranston, E. D., Eichhorn, S. J., Fox, D. M., Hamad, W. Y., Heux, L., Jean, B., Korey, M., Nieh, W., Ong, K. J., Reid, M. S., Renneckar, S., … Youngblood, J. (2018). Current characterization methods for cellulose nanomaterials. *Chemical Society Reviews*, *47*(8), 2609–2679. https://doi.org/10.1039/C6CS00895J

Fraggedakis, D., Dimakopoulos, Y., & Tsamopoulos, J. (2016). Yielding the yield stress analysis: A thorough comparison of recently proposed elasto-visco-plastic (EVP) fluid models. *Journal of Non-Newtonian Fluid Mechanics*, *236*, 104–122. https://doi.org/10.1016/j.jnnfm.2016.09.001

Gómez H., C., Serpa, A., Velásquez-Cock, J., Gañán, P., Castro, C., Vélez, L., & Zuluaga, R. (2016). Vegetable nanocellulose in food science: A review. *Food Hydrocolloids*, *57*, 178–186. https://doi.org/10.1016/j.foodhyd.2016.01.023

Guiraud, O., Dumont, P. J. J., & Orgéas, L. (2013). How to Prepare SMC and BMC-like Compounds to Perform Relevant Rheological Experiments? *Applied Composite Materials*, *20*(2), 157–169. https://doi.org/10.1007/s10443-012-9261-z

Guiraud, O., Dumont, P. J. J., Orgéas, L., & Favier, D. (2012). Rheometry of compression moulded fibre-reinforced polymer composites: Rheology, compressibility, and friction forces with mould surfaces. *Composites Part A: Applied Science and Manufacturing*, *43*(11), 2107–2119. https://doi.org/10.1016/j.compositesa.2012.06.006

Gupta, S., Martoïa, F., Orgéas, L., & Dumont, P. J. J. (2018). Ice-Templated Porous Nanocellulose-Based Materials: Current Progress and Opportunities for Materials Engineering. *Applied Sciences*, *8*(12), 2463. https://doi.org/10.3390/app8122463

Hausmann, M. K., Rühs, P. A., Siqueira, G., Läuger, J., Libanori, R., Zimmermann, T., & Studart, A. R. (2018). Dynamics of Cellulose Nanocrystal Alignment during 3D Printing. *ACS Nano*, *12*(7), 6926–6937. https://doi.org/10.1021/acsnano.8b02366

Hubbe, M. A., Tayeb, P., Joyce, M., Tyagi, P., Kehoe, M., Dimic-Misic, K., & Pal, L. (2017). Rheology of Nanocellulose-rich Aqueous Suspensions: A Review. *BioResources*, *12*(4), 9556-9661–9661. https://doi.org/10.15376/biores.12.4.9556-9661

Isogai, A., Saito, T., & Fukuzumi, H. (2011). TEMPO-oxidized cellulose nanofibers. *Nanoscale*, *3*(1), 71–85. https://doi.org/10.1039/C0NR00583E

Jiang, F., & Hsieh, Y.-L. (2013). Super water absorbing and shape memory nanocellulose aerogels from TEMPO-oxidized cellulose nanofibrils via cyclic freezing–thawing. *Journal of Materials Chemistry A*, *2*(2), 350–359. https://doi.org/10.1039/C3TA13629A

Jiang, F., & Hsieh, Y.-L. (2014). Amphiphilic superabsorbent cellulose nanofibril aerogels. *Journal of Materials Chemistry A*, *2*(18), 6337–6342. https://doi.org/10.1039/C4TA00743C

Keshavarz, B., Divoux, T., Manneville, S., & McKinley, G. H. (2017). Nonlinear Viscoelasticity and Generalized Failure Criterion for Polymer Gels. *ACS Macro Letters*, *6*(7), 663–667. https://doi.org/10.1021/acsmacrolett.7b00213

Kettunen, M., Silvennoinen, R. J., Houbenov, N., Nykänen, A., Ruokolainen, J., Sainio, J., Pore, V., Kemell, M., Ankerfors, M., Lindström, T., Ritala, M., Ras, R. H. A., & Ikkala, O. (2011). Photoswitchable Superabsorbency Based on Nanocellulose Aerogels. *Advanced Functional Materials*, *21*(3), 510–517. https://doi.org/10.1002/adfm.201001431

Klemm, D., Cranston, E. D., Fischer, D., Gama, M., Kedzior, S. A., Kralisch, D., Kramer, F., Kondo, T., Lindström, T., Nietzsche, S., Petzold-Welcke, K., & Rauchfuß, F. (2018). Nanocellulose as a natural source for groundbreaking applications in materials science: Today's state. *Materials Today*, *21*(7), 720–748. https://doi.org/10.1016/j.mattod.2018.02.001

Li, A., Xu, D., Luo, L., Zhou, Y., Yan, W., Leng, X., Dai, D., Zhou, Y., Ahmad, H., Rao, J., & Fan, M. (2021). Overview of nanocellulose as additives in paper processing and paper products. *Nanotechnology Reviews*, *10*(1), 264–281. https://doi.org/10.1515/ntrev-2021-0023

Lundahl, M. J., Berta, M., Ago, M., Stading, M., & Rojas, O. J. (2018). Shear and extensional rheology of aqueous suspensions of cellulose nanofibrils for biopolymer-assisted filament spinning. *European Polymer Journal*, *109*, 367–378. https://doi.org/10.1016/j.eurpolymj.2018.10.006

Lundahl, M. J., Klar, V., Wang, L., Ago, M., & Rojas, O. J. (2017). Spinning of Cellulose Nanofibrils into Filaments: A Review. *Industrial & Engineering Chemistry Research*, *56*(1), 8–19. https://doi.org/10.1021/acs.iecr.6b04010

Martoïa, F., Dumont, P. J. J., Orgéas, L., Belgacem, M. N., & Putaux, J.-L. (2016a). Micro-mechanics of electrostatically stabilized suspensions of cellulose nanofibrils under steady state shear flow. *Soft Matter*, *12*(6), 1721–1735. https://doi.org/10.1039/C5SM02310F

Martoïa, F., Dumont, P. J. J., Orgéas, L., Belgacem, M. N., & Putaux, J.-L. (2016b). On the origins of the elasticity of cellulose nanofiber nanocomposites and nanopapers: A micromechanical approach. *RSC Advances*, *6*(53), 47258–47271. https://doi.org/10.1039/C6RA07176G

Martoïa, F., Gupta, S., Dumont, P. J. J., & Orgéas, L. (2022). Rheology of concentrated and highly concentrated enzymatic cellulose nanofibril hydrogels during lubricated compression. *Carbohydrate Polymers*, *296*, 119911. https://doi.org/10.1016/j.carbpol.2022.119911

Martoïa, F., Perge, C., Dumont, P. J. J., Orgéas, L., Fardin, M. A., Manneville, S., & Belgacem, M. N. (2015). Heterogeneous flow kinematics of cellulose nanofibril suspensions under shear. *Soft Matter*, *11*(24), 4742–4755. https://doi.org/10.1039/C5SM00530B

Masruchin, N., Park, B.-D., Causin, V., & Um, I. C. (2015). Characteristics of TEMPO-oxidized cellulose fibril-based hydrogels induced by cationic ions and their properties. *Cellulose*, *22*(3), 1993–2010. https://doi.org/10.1007/s10570-015-0624-0

McKee, J. R., Appel, E. A., Seitsonen, J., Kontturi, E., Scherman, O. A., & Ikkala, O. (2014). Healable, Stable and Stiff Hydrogels: Combining Conflicting Properties Using Dynamic and Selective Three-Component Recognition with Reinforcing Cellulose Nanorods. *Advanced Functional Materials*, *24*(18), 2706–2713. https://doi.org/10.1002/adfm.201303699

Meftahi, A., Samyn, P., Geravand, S. A., Khajavi, R., Alibkhshi, S., Bechelany, M., & Barhoum, A. (2022). Nanocelluloses as skin biocompatible materials for skincare, cosmetics, and healthcare:

Formulations, regulations, and emerging applications. *Carbohydrate Polymers*, *278*, 118956. https://doi.org/10.1016/j.carbpol.2021.118956

Moberg, T., Rigdahl, M., Stading, M., & Levenstam Bragd, E. (2014). Extensional viscosity of microfibrillated cellulose suspensions. *Carbohydrate Polymers*, *102*, 409–412. https://doi.org/10.1016/j.carbpol.2013.11.041

Nechyporchuk, O., Belgacem, M. N., & Bras, J. (2016). Production of cellulose nanofibrils: A review of recent advances. *Industrial Crops and Products*, *93*, 2–25. https://doi.org/10.1016/j.indcrop.2016.02.016

Nechyporchuk, O., Belgacem, M. N., & Pignon, F. (2016). Current Progress in Rheology of Cellulose Nanofibril Suspensions. *Biomacromolecules*, *17*(7), 2311–2320. https://doi.org/10.1021/acs.biomac.6b00668

Orgéas, L., Dumont, P. J. J., Le, T.-H., & Favier, D. (2008). Lubricated compression of BMC, a concentrated and fibre-reinforced granular polymer suspension. *Rheologica Acta*, *47*(5), 677. https://doi.org/10.1007/s00397-008-0276-1

Reid, M. S., Villalobos, M., & Cranston, E. D. (2017). Benchmarking Cellulose Nanocrystals: From the Laboratory to Industrial Production. *Langmuir*, *33*(7), 1583–1598. https://doi.org/10.1021/acs.langmuir.6b03765

Rol, F., Karakashov, B., Nechyporchuk, O., Terrien, M., Meyer, V., Dufresne, A., Belgacem, M. N., & Bras, J. (2017). Pilot-Scale Twin Screw Extrusion and Chemical Pretreatment as an Energy-Efficient Method for the Production of Nanofibrillated Cellulose at High Solid Content. *ACS Sustainable Chemistry & Engineering*, *5*(8), 6524–6531. https://doi.org/10.1021/acssuschemeng.7b00630

Saito, T., Kimura, S., Nishiyama, Y., & Isogai, A. (2007). Cellulose Nanofibers Prepared by TEMPO-Mediated Oxidation of Native Cellulose. *Biomacromolecules*, *8*(8), 2485–2491. https://doi.org/10.1021/bm0703970

Saito, T., Nishiyama, Y., Putaux, J.-L., Vignon, M., & Isogai, A. (2006). Homogeneous Suspensions of Individualized Microfibrils from TEMPO-Catalyzed Oxidation of Native Cellulose. *Biomacromolecules*, *7*(6), 1687–1691. https://doi.org/10.1021/bm060154s

Saramito, P. (2007). A new constitutive equation for elastoviscoplastic fluid flows. *Journal of Non-Newtonian Fluid Mechanics*, *145*(1), 1–14. https://doi.org/10.1016/j.jnnfm.2007.04.004

Saramito, P. (2009). A new elastoviscoplastic model based on the Herschel–Bulkley viscoplastic model. *Journal of Non-Newtonian Fluid Mechanics*, *158*(1), 154–161. https://doi.org/10.1016/j.jnnfm.2008.12.001

Shafeiei-Sabet, S., Hamad, W. Y., & Hatzikiriakos, S. G. (2013). Influence of degree of sulfation on the rheology of cellulose nanocrystal suspensions. *Rheologica Acta*, *52*(8), 741–751. https://doi.org/10.1007/s00397-013-0722-6

Toll, S. (1993). Note: On the tube model for fiber suspensions. *Journal of Rheology*, *37*(1), 123–125. https://doi.org/10.1122/1.550460

Ureña-Benavides, E. E., Ao, G., Davis, V. A., & Kitchens, C. L. (2011). Rheology and Phase Behavior of Lyotropic Cellulose Nanocrystal Suspensions. *Macromolecules*, *44*(22), 8990–8998. https://doi.org/10.1021/ma201649f

Wang, Q., Yao, Q., Liu, J., Sun, J., Zhu, Q., & Chen, H. (2019). Processing nanocellulose to bulk materials: A review. *Cellulose*, *26*(13), 7585–7617. https://doi.org/10.1007/s10570-019-02642-3

Zakani, B., & Grecov, D. (2020). Yield stress analysis of cellulose nanocrystalline gels. *Cellulose*, *27*(16), 9337–9353. https://doi.org/10.1007/s10570-020-03429-7

Zakani, B., & Grecov, D. (2022). Effect of ultrasonic treatment on yield stress of highly concentrated cellulose nano-crystalline (CNC) aqueous suspensions. *Carbohydrate Polymers*, *291*, 119651. https://doi.org/10.1016/j.carbpol.2022.119651